

THE ROLE OF MAGNETIC HELICITY IN CORONAL HEATING

K. J. KNIZHNIK¹, S. K. ANTIOCHOS², J. A. KLIMCHUK² AND C. R. DEVORE²

September 10, 2019

ABSTRACT

One of the greatest challenges in solar physics is understanding the heating of the Sun’s corona. Most theories for coronal heating postulate that free energy in the form of magnetic twist/stress is injected by the photosphere into the corona where the free energy is converted into heat either through reconnection or wave dissipation. The magnetic helicity associated with the twist/stress, however, is expected to be conserved and appear in the corona. In previous work we showed that helicity associated with the small-scale twists undergoes an inverse cascade via stochastic reconnection in the corona, and ends up as the observed large-scale shear of filament channels. Our “helicity condensation” model accounts for both the formation of filament channels and the observed smooth, laminar structure of coronal loops. In this paper, we demonstrate, using helicity- and energy-conserving numerical simulations of a coronal system driven by photospheric motions, that the model also provides a natural mechanism for heating the corona. We show that the heat generated by the reconnection responsible for the helicity condensation process is sufficient to account for the observed coronal heating. We study the role that helicity injection plays in determining coronal heating and find that, crucially, the heating rate is only weakly dependent on the net helicity preference of the photospheric driving. Our calculations demonstrate that motions with 100% helicity preference are least efficient at heating the corona; those with 0% preference are most efficient. We discuss the physical origins of this result and its implications for the observed corona.

Keywords: Sun: corona – Sun: coronal heating – Sun: magnetic fields

1. INTRODUCTION

Understanding the nature of coronal heating is a long-standing problem in solar physics dating back to the work of [Grotrian \(1939\)](#), who discovered that coronal temperatures are in excess of 10^6 K, approximately two orders of magnitude hotter than the underlying photosphere. Calculations by [Withbroe & Noyes \(1977\)](#) showed that the energy flux necessary to account for the observed temperatures is of order 1×10^7 ergs $\text{cm}^{-2} \text{s}^{-1}$ in active regions and 3×10^5 ergs $\text{cm}^{-2} \text{s}^{-1}$ in quiet Sun. Explaining the mechanism for the heating has been, to some extent, the central unsolved problem in solar physics ([Parker 1972](#); [Klimchuk 2006, 2015](#)).

While it is generally agreed that the energy must ultimately come from the photosphere and below, there are two main mechanisms that are frequently used to explain the observed heating. [Parker \(1972\)](#) argued that quasi-static photospheric motions tangle, twist, and braid the magnetic field, imparting it with magnetic free energy, which is then converted into heat by magnetic reconnection. Such reconnection events, frequently called nanoflares (e.g. [Parker 1972, 1983](#); [Cargill 1994](#); [Klimchuk 2006, 2015](#)), are thought to occur between elemental strands, perhaps as small as 15 km in diameter ([Peter et al. 2013](#)). An alternative explanation for the heating is that waves, such as the Alfvén ([Osterbrock 1961](#)) or magnetosonic ([Pekünlü et al. 2001](#)) modes, are generated by photospheric processes and deposit their energy into the corona by resonant absorption, phase mixing, or turbulent dissipation.

These models are frequently able to quantitatively reproduce the observed heating (e.g., [Kumar et al. 2006](#); [Viall & Klimchuk 2011](#); [Bradshaw et al. 2012](#); [Hahn & Savin 2014](#), see, however, [González-Avilés & Guzmán 2015](#)), but to date there has been little consideration of their topological implications. Incessant jostling of the magnetic-field footpoints in the photosphere causes the coronal field to become tangled and twisted, thereby injecting helicity. There is, however, little observational evidence for significant helicity, at least on large scales. The corona has a rather simple, laminar appearance in images ranging from the visible, to EUV, to soft X-ray ([Schrijver et al. 1999](#)). With very few exceptions ([Cirtain et al. 2013](#)), coronal loops — defined here as observationally distinct structures — seem to be well aligned and to not wrap around each other. Complexity must be present on sub-resolution scales, however, otherwise it would not be possible to dissipate sufficient magnetic energy to account for the observed coronal heating. Furthermore, complexity may be present within the highly important diffuse component of the corona that exists between loops ([Viall & Klimchuk 2011](#)), but the level of topological complexity that one might expect to accumulate on large observable scales due to the injected helicity does not seem to exist.

One might argue that the expected complexity is simply removed by magnetic reconnection. However, resolving the issue in this way is not straightforward. In the high Lundquist-number regime of the solar corona, magnetic helicity is conserved under reconnection ([Woltjer 1958](#); [Taylor 1974, 1986](#); [Berger 1984](#)). Reconnection rearranges the helicity but does not destroy it. Some process must remove the helicity from where it is locally injected, in order to avoid buildup of tangling and braiding.

¹Naval Research Laboratory, 4555 Overlook Avenue SW, Washington, DC 20375 USA

²Heliophysics Science Division, NASA Goddard Space Flight Center, Greenbelt, Maryland

We have recently described such a process. As a result of “helicity condensation” (Antiochos 2013), magnetic twist naturally migrates via magnetic reconnection to polarity inversion lines (PILs), where it manifests as sheared filament channels (Zhao et al. 2015). Using helicity-conserving MHD simulations, we showed that helicity condensation produces strong concentrations of shear at PILs, and leaves behind a generally smooth corona with well-aligned coronal loops (Knizhnik et al. 2015, hereafter KAD15). Subsequently, we demonstrated that this process occurs even if a fraction of the helicity injected into the corona has a sign opposite to that of the dominant helicity injection (Knizhnik et al. 2017a, hereafter KAD17). Varying the fraction of positive/negative helicity affects both the time scale of filament channel formation and the amount of structure in the smooth-loop corona. In particular, if there is a 3:1 ratio of positive/negative helicity, as appears to be the case in the corona (Pevtsov et al. 2003), filament channels will form in about a day. On the other hand, a 1:1 ratio of positive/negative helicity injection will preclude the formation of filament channels altogether and, counter-intuitively, result in a more complex corona than is generally observed. The helicity condensation process, therefore, naturally explains why strong shear/twist is not observed in the closed corona except in filament channels.

Although these results have shown that magnetic reconnection transports magnetic helicity to PILs by removing it from the coronal loops, it is not clear how much energy is converted to heat in this process. Filament channels are highly sheared structures that contain a large amount of free energy, which must have come, at least in part, from the energy injected at the photosphere. Welsch (2015) measured the Poynting flux injected from the photospheric level into the coronal field, and found values well in line with the prediction of Withbroe & Noyes (1977). However, not all of the energy injected is converted to volumetric heating, as a large amount of the energy remains in the coronal field in the form of filament channels. Furthermore, it is not obvious that the conversion of magnetic energy into heat is efficient enough to account for the observed heating. Quantifying precisely how much of the Poynting flux is converted into heat by magnetic reconnection, therefore, is crucial to testing the helicity condensation model and understanding the energy source of the multi-million degree corona.

Photospheric flows inject both magnetic helicity and free energy into the coronal field. In contrast to helicity injection, which depends only on the normal component of the magnetic field at the photosphere, energy injection depends on both the normal and horizontal components. In the absence of flux emergence, the normal component of the magnetic field can be readily determined, because it simply convects with the ideal photospheric flow. The horizontal component of the magnetic field, on the other hand, is much harder to measure observationally. Knowing the velocity distribution on the photosphere is not sufficient to determine the evolution of the horizontal component of the field, because magnetic reconnection in the corona removes stress from the field, which is then able to relax along the entire length of its field lines. This effect changes the horizontal components of the field at the photosphere, implying that the Poynting flux is not determined solely by the driver velocity, but by a com-

plicated feedback between photospheric motions and the coronal response. Thus, while helicity injection can be computed directly from the dynamics observed or imposed at the photosphere, energy injection requires computation of the detailed coronal dynamics.

The interplay between photospheric stressing, magnetic reconnection, and the subsequent energy release and relaxation has been investigated by many authors. Rappazzo et al. (2013) studied energy injection into a plane-parallel coronal geometry by photospheric twisting motions. They analyzed the turbulent cascade that resulted from a large-scale photospheric driver and found that field lines developed a complex twisted topology and released energy by reconnecting at many small-scale current sheets. In addition to the transfer of energy from large scales to small, they found that an inverse energy cascade also took place. They demonstrated that on long time scales most of the free magnetic energy was stored at the largest possible scales. Wilmot-Smith et al. (2011) used resistive MHD simulations to investigate braiding of a plane-parallel corona by photospheric motions and found that heating of the corona via magnetic reconnection is crucially dependent on the nature of these motions. Furthermore, they argued that injecting large amounts of magnetic helicity does not increase the amount of energy available for conversion to heat, compared to injecting less helicity, because the resulting minimum-energy state determined by helicity conservation will itself have a higher energy. In all cases, however, the relaxation that follows magnetic reconnection results in a complex distribution of current sheets, which can themselves dissipate and release further energy (Pontin et al. 2011; Dahlburg et al. 2016).

In this paper, we show that the magnetic reconnection responsible for “condensing” magnetic helicity onto the PIL converts the majority of the injected magnetic energy into plasma heating at a rate sufficient to sustain the observed coronal temperatures. Furthermore, we find the surprising result that the coronal heating due to this process is only weakly dependent on the helicity injection preference, even though for large net helicity injection a significant amount of magnetic energy remains stored in the large-scale shear observed in filament channels. This work, combined with the results of KAD15 and KAD17, demonstrates that the helicity condensation model provides a self-consistent explanation for both the structure and heating of the corona. Magnetic energy and helicity are injected at the photosphere, but whereas the helicity condenses to form concentrated filament channels at PILs, magnetic energy is everywhere converted into heat by magnetic reconnection. Thus, understanding the transport of magnetic helicity throughout the corona is crucial to understanding solar coronal heating.

The paper is organized as follows. In §2 we review the setup of our numerical simulations. In §3 we discuss the results, describing the partitioning of injected energy into magnetic and internal energy and how the resolution of the simulations affects our findings. In §5 we relate the numerical values from our simulations to coronal measurements. Finally, in §6 we present our conclusions and their implications for future research.

2. NUMERICAL MODEL

We solve the equations of magnetohydrodynamics (MHD) using the Adaptively Refined Magnetohydrodynamics Solver (ARMS; DeVore & Antiochos 2008) in three Cartesian dimensions. The equations have the form

$$\frac{\partial \rho}{\partial t} + \nabla \cdot \rho \mathbf{v} = 0, \quad (2.1)$$

$$\frac{\partial \rho \mathbf{v}}{\partial t} + \nabla \cdot (\rho \mathbf{v} \mathbf{v}) = -\nabla P + \frac{1}{4\pi} (\nabla \times \mathbf{B}) \times \mathbf{B}, \quad (2.2)$$

$$\frac{\partial E}{\partial t} + \nabla \cdot \left\{ \left(E + P + \frac{B^2}{8\pi} \right) \mathbf{v} - \frac{\mathbf{B}(\mathbf{v} \cdot \mathbf{B})}{4\pi} \right\} = 0, \quad (2.3)$$

$$\frac{\partial \mathbf{B}}{\partial t} = \nabla \times (\mathbf{v} \times \mathbf{B}), \quad (2.4)$$

where

$$E = U + K + M \quad (2.5)$$

is the total energy density, the sum of the internal energy density

$$U = \frac{P}{\gamma - 1}, \quad (2.6)$$

kinetic energy density

$$K = \frac{\rho v^2}{2}, \quad (2.7)$$

and magnetic energy density

$$M = \frac{B^2}{8\pi}. \quad (2.8)$$

In these equations, ρ is mass density, T is temperature, P is thermal pressure, $\gamma = 5/3$ is the ratio of specific heats, \mathbf{v} is velocity, \mathbf{B} is magnetic field, and t is time. We close the equations via the ideal gas law,

$$P = \rho RT, \quad (2.9)$$

where R is the gas constant.

ARMS uses finite-volume representations of the variables to solve the system of equations. Its Flux Corrected Transport algorithms (DeVore 1991) provide minimal, though finite, numerical dissipation, which allows magnetic reconnection to occur. As a result, ARMS conserves the magnetic helicity in the system to an excellent approximation, even when reconnection occurs throughout a substantial fraction of the total volume (Knizhnik et al. 2015; Knizhnik et al. 2017a; Knizhnik et al. 2017b; Knizhnik et al. 2018).

The homogeneity of the system of MHD equations (2.1)-(2.4) allows us to scale out characteristic values of mass, length, and time (or equivalent combinations of these fundamental units) and solve the equations in non-dimensional form. We do this by extracting values of length L_s , mass density ρ_s , and magnetic-field strength B_s that can be specified later to convert our non-dimensional numerical values into solar values appropriate to different portions of the atmosphere (active region, quiet Sun).

Following Parker's (1972) original *ansatz*, we set up a model coronal field that is initially straight and uniform between two plates, as shown in Figure 1. In this model, straight flux tubes represent coronal loops whose apex is located in the center of the domain, and the top and

bottom boundaries represent the photosphere. At all six boundaries, we apply zero-gradient conditions to ρ , E , and \mathbf{B} . The four side walls are open, with zero-gradient conditions applied to \mathbf{v} , but due to the form of the driver discussed below, we find that the velocities at these side walls are negligible throughout all the simulations. The top and bottom boundaries are closed, where we set the normal flow component $v_x = 0$ and specify the tangential components v_y, v_z as described below. These imposed boundary flows mimic driving at the plasma-dominated photosphere where the magnetic field is line-tied.

Our domain is $[0, L_x] \times [-L_y, L_y] \times [-L_z, L_z]$, where x is normal to the photosphere (the vertical direction). We set $L_x = 1$ and $L_y = L_z = 1.5$. The domain is spanned initially by a grid of $4 \times 12 \times 12$ blocks, where each block consists of $8 \times 8 \times 8$ finite-volume cells. The grid was refined up to three additional levels above this base resolution, for four total refinement levels $l = 1, 2, 3$, and 4. The main results presented in the next section were obtained on the $l = 3$ grid, whose effective uniform size was $128 \times 384 \times 384$.

We set the initial, uniform values in our non-dimensional simulations to $\rho_0 = 1$, $T_0 = 1$, $P_0 = 0.1$, and $B_0 = \sqrt{4\pi}$. These choices set the sound speed, $c_{S0} = \sqrt{\gamma P_0 / \rho_0} = 0.4$, Alfvén speed, $c_{A0} = B_0 / \sqrt{4\pi \rho_0} = 1$, and plasma beta (ratio of thermal to magnetic pressure), $\beta_0 = 8\pi P_0 / B_0^2 = 0.2$. $\beta \ll 1$ corresponds to a magnetically dominated plasma, and this condition generally holds in the corona. The results presented below are given in simulation time, which is normalized to the (unit) time required for an Alfvén wave at ambient speed to propagate between the top and bottom plates ($t_{A0} = L_x / c_{A0} = 1$).

As with our earlier studies, we inject helicity in the form of localized vortices over a finite region to approximate a finite polarity region bounded by a PIL. Such vortices are observed in the photosphere at the boundaries between convection cells (Duvall & Gizon 2000; Gizon & Duvall 2003; Komm et al. 2007; Bonet et al. 2008; Seligman et al. 2014; Vargas Domínguez et al. 2015). Furthermore, turbulent photospheric convection produces random flows, which can always be deconvolved into translational and rotational components. For simplicity, we approximate these flows with a rotational pattern, described below, that allows for easy adjustment of the helicity injection rate while maintaining the random nature of the flow. As in KAD17, we impose a photospheric hexagonal pattern of $N = 61$ cellular rotations (shown in Fig. 1) that is randomly shifted by an arbitrary angle after each complete cycle of twist. Each such cycle consists of a sinusoidal ramp-up and ramp-down, with the angular velocity of each individual cell taking the form

$$\Omega(r, t) = -\Omega_0 g(r) f(t) \quad (2.10)$$

where

$$g(r) = \left(\frac{r}{a_0} \right)^4 - \left(\frac{r}{a_0} \right)^8 \quad (2.11)$$

and

$$f(t) = \frac{1}{2} \left[1 - \cos \left(2\pi \frac{t}{\tau} \right) \right]. \quad (2.12)$$

Here, r is the cylindrical coordinate on the plane boundary measured from the center of the cell, limited to the

interval $r \in [0, a_0]$ in Eq. 2.11. This flow is incompressible and leaves the vertical magnetic field component B_x undisturbed; the tangential field component \mathbf{B}_h , on the other hand, is free to adjust in response to the imposed surface flows and to the dynamics occurring in the coronal volume above. The zero-gradient conditions allow any change in \mathbf{B}_h in the interior to propagate to and appear at the boundary, so that any accumulation of \mathbf{B}_h at the boundaries and in the volume is fundamentally due to coronal reconnection and not a direct result of boundary motions. We set the flow amplitude $\Omega_0 = 7.5$, the flow radius $a_0 = 0.125$, and the flow period $\tau = 3.35$, which yield a maximum angle of rotation within the cell $\phi_{max} = \pi$ and a maximum flow speed $v_h^{max} = 0.2$. The twisting is applied on both the top and bottom plates, so the maximum rotation angle of each flux tube is 2π . Each simulation is run out for 20 twist cycles, which are followed by 5 relaxation cycles during which no further twisting motions are applied.

In addition to randomly rotating the hexagonal pattern from cycle to cycle, two of our simulations further randomize the energy and helicity injection into the corona by randomizing the sense of rotation (clockwise or counter-clockwise) of the individual cells after each cycle. As described in KAD17, our three simulations presented below correspond to net preferences p of 100%, 50%, and 0% for clockwise (positive-helicity) rotations. In the first case, all rotations are clockwise; in the third case, half are clockwise and half counter-clockwise; and in the second, the ratio of clockwise to counter-clockwise rotations is 3:1. A key point is that even though our imposed motions consist of simple rotations, the random rotation of the flow pattern implies that the effective driving is fully chaotic, like actual solar convective flows. Any one point at the photosphere moves along an unpredictable chaotic path. Consequently, our imposed driving captures the essential features of the convective turbulence while allowing for simple adjustment of the helicity injection rate.

The key difference between the present study and our previous work (KAD15, KAD17) is that here we solve Eq. 2.3 to conserve total energy during the evolution. In our previous simulations, we solved the adiabatic temperature equation, and all changes in the internal energy density were due to compression or expansion. These two descriptions are equivalent if the evolution is purely ideal. However, the numerical diffusion terms in the momentum and induction equations provide finite viscous and resistive damping, respectively, that produces localized heating. With the adiabatic approximation these heating terms are simply lost. By solving the conservative form of the total energy equation, on the other hand, we capture the full heating. Our energy equation is still an approximation for the actual corona: no thermal conduction or radiation is included in our simulations. Consequently, all temperature increases due to the viscous and resistive heating simply accumulate monotonically. Nevertheless, by capturing rigorously the conversion of kinetic and magnetic energy into plasma energy during reconnection, we are able to assess quantitatively the amount of coronal heating that occurs in our simulations and how that varies for different helicity injection preferences and other parameters.

3. RESULTS

We present several diagnostics that quantify the heating of the corona for each of our simulations with varying helicity injection preferences, beginning with the final temperature distributions. Then we focus on the energetics addressing, in turn, the Poynting fluxes and the volumetric energies – magnetic, internal, and total. Finally, we show and discuss the effects of grid resolution (i.e., the effective Lundquist number) on our results.

3.1. Temperature

As an initial assessment of the coronal heating implied by the helicity condensation model, we plot the temperature in the mid-plane of the domain at the end of each simulation in Figure 2. The contours show the ratio of the final temperature to the initial temperature, $T_0 = 1$. Since we apply closed boundary conditions at the top and bottom of the domain, and the motions at the side walls remain very small, the total mass is conserved throughout the evolution. Consequently, any heating results primarily in an increase in temperature. The temperature map, therefore, is a fairly accurate indicator of the spatial distribution of the time-integrated heating over the domain. There are some changes in plasma density, however, due to the formation of the filament channel and the resulting expansion of the flux in that region balanced by compression in the surrounding. To illustrate those changes, we also show in Figure 2 the vertical magnetic field at the midplane relative to its initial value. Any increase (decrease) of this field from its initially uniform strength $B_0 = \sqrt{4\pi}$ indicates a local contraction (expansion) there.

The first feature to note is that, in all cases, the temperature and the vertical field exhibit a sharp jump between the driven and undriven regions. This is to be expected given that the driving pattern of Figure 1 has a nearly discontinuous boundary for any one rotation cycle. The fact that we randomly rotate the whole pattern creates a finite interface between the driven and undriven regions, but its width is only of order a fraction of a rotation cell. Figure 2 shows that there is minimal spreading of the injected twist field, whether due to reconnection or to numerical diffusion.

The second important feature is that the temperature reaches its maximum near the center of the driven region, and it is approximately the same in all three cases. This result implies that the amount of magnetic energy dissipated by reconnection is roughly constant, even though the net helicity injection rate is very different in the three cases. We discuss this key finding in more detail below. Furthermore, in all cases the central region does not exhibit any pronounced large-scale structure. Two caveats, however, need to be noted here when applying our results to the actual corona. First, our model corona has artificial uniformity in that the normal field at the photosphere is constant and all the field lines have the same length. In the true corona, both the photospheric field and the field-line length vary, which naturally results in observed systematic temperature variations. Second, there is no heat loss via radiation in our corona, so that the plasma beta becomes artificially large. From Figure 2, we note that the temperature at the center has increased by almost an order of magnitude, which implies

that the beta there has risen significantly above unity. In the real corona, the plasma is always low beta and is continuously cooling and heating, which at any instant results in strong cross-field temperature variations.

On the other hand, the lack of substantial structure in the magnetic-field contours agrees well with the many observations that the coronal field appears largely smooth and laminar (Schrijver et al. 1999). The central portion of our driven region corresponds to the bulk of the observed closed corona: coronal loops outside of filament channels. It is evident from Figure 2 that the central region is even smoother in the case with 100% helicity injection than in that with net zero helicity injection. This may seem counter-intuitive, because one might expect to see evidence of the large helicity injection. In fact, however, we have found (KAD17) that a 100% helicity injection preference consistently leads to a coronal magnetic field outside filament channels that exhibits the least amount of large-scale structure. This occurs because, in the 100% case, the helicity condensation process is most efficient at transporting the injected magnetic twist to the PIL, where it builds up the sheared filament channel.

Although the central parts of the driven regions are fairly similar in the three cases, the boundaries clearly exhibit systematic differences. This is to be expected, because these boundaries separate the twisted and untwisted flux systems, and so act analogously to PILs: filament channels can form there, but only if a nonzero net helicity is injected into the corona (e.g., Zhao et al. 2015; Knizhnik et al. 2015; Knizhnik et al. 2017a; Knizhnik et al. 2017b). First, we note from Figure 2 that throughout the driven region, the vertical field B_x is smaller than its initial value $B_0 = 1$. This is due to significant horizontal field components, B_y and B_z , that have been generated in this region by the photospheric motions. The extra magnetic pressure contributed by the horizontal field causes the driven region to expand outward, especially at the midplane, thereby lowering the average vertical field strength. For the 0% helicity injection case, the vertical field is roughly uniform throughout the driven region, indicating that the magnitude (but not the sign) of the horizontal field is also roughly uniform there. The 100% case, however, shows a much different structure. The vertical field exhibits a ring of large expansion at the boundary – the “PIL” – due to the buildup of very strong horizontal field, i.e., the sheared filament channel. In fact, the maximum magnitude of the horizontal field is more than twice as large as the local vertical field magnitude. This ratio is in line with that in true filaments, where the horizontal field is measured to be up to an order of magnitude larger than the vertical field (Mackay et al. 2010). Due to the concentration of the shear field in the filament channel, the interior region of the 100% case exhibits less expansion and weaker horizontal field than in the 0% case, showing again that the 100% case is most efficient at eliminating the horizontal (shear) flux by condensing it at the PIL. The ring of large field expansion results in a ring of lower temperature at the boundary of the 100% case. (We emphasize here that this temperature decrease has no relation to the physical process by which filament channels acquire cool plasma.) Note also that the 100% case exhibits a weak remnant of the hexagonal photospheric driving pattern (Fig. 1) in the

magnetic field and temperature. This weak effect is not present in the other cases due to the greater randomness of their photospheric twisting motions.

3.2. Poynting Flux

The imposed footpoint motions in our simulations inject energy principally into the magnetic field. There is an attendant injection of kinetic energy associated directly with the motions, but this energy contribution is very small, of order 10^{-4} times that of the magnetic energy. The Poynting flux density of electromagnetic energy (i.e., energy per unit area per unit time) at any location within the domain is

$$\begin{aligned} \mathbf{S} &= \frac{c}{4\pi} [\mathbf{E} \times \mathbf{B}] \\ &= -\frac{1}{4\pi} [(\mathbf{v} \times \mathbf{B}) \times \mathbf{B}]. \end{aligned} \quad (3.1)$$

The fluxes at the domain boundaries determine the energy added to, or subtracted from, the total volume. The fluxes at the side walls are negligible, because the outflows there are very small. The fluxes at the top and bottom boundaries are due solely to the imposed horizontal footpoint flows \mathbf{v}_h , because the normal velocity component v_n is held fixed at zero. Thus, the normal component of the Poynting flux density at the top and bottom boundaries is given by

$$S_n(y, z, t) = -\frac{1}{4\pi} B_n (\mathbf{v}_h \cdot \mathbf{B}_h), \quad (3.2)$$

and it is the source of essentially all the energy added to the volume during the simulation. Note also that this energy is all free energy because the imposed motions are incompressible, so the uniform normal flux at the boundary does not change throughout the simulation. Hence, the reference potential field is constant.

Figure 3 shows the Poynting flux density S_n on the bottom plate at the peaks of the first and last cycles for each of the three cases. The flux depends upon the stress exerted by the field on the surface, which for our case varies only with the horizontal field component \mathbf{B}_h , because the vertical field is constant. Slow twisting of field lines by the convective flow \mathbf{v}_h does work on the field, injecting energy at a rate determined by $\mathbf{v}_h \cdot \mathbf{B}_h$. This stress can be partially relieved by the rearrangement of field lines due to reconnection in the overlying corona. As expected, the Poynting flux density during the first cycle is identical for the three cases, and corresponds exactly to the rotational cell pattern in the photosphere (Fig. 3a). Early on, before the onset of any reconnection, the only effect of the motions is to inject twist (horizontal) flux into each flux tube driven by a rotational cell. The energy associated with this twist flux is independent of the sign of the twist (clockwise or counter-clockwise); consequently, the Poynting flux is everywhere positive, and is essentially identical in each rotation cell. In principle, there is some variation due to the fact that the twisted flux tubes at the periphery of the driving pattern can expand more than those in the interior, but this effect is extremely small.

The situation is very different later in the simulation. The field acquires a complex distribution of horizontal flux, and the magnetic stress at the photosphere can either oppose or reinforce the motion. If it opposes, then

the flow does work on the field and there is a positive injection of magnetic energy. If the stress and the motion are in the same direction, then energy is removed from the field as it de-stresses, and the Poynting flux density is negative. The field, of course, also de-stresses due to reconnection in the volume.

Panels (b), (c), and (d) in Figure 3 show the Poynting flux in the middle of the last cycle for the three helicity injection preferences. As discussed above, the flux density has both positive and negative regions, but a preponderance of positive. We note that the maximum flux is a factor of 3 or so greater than that halfway through the first cycle. Since the velocities at the photosphere have fixed magnitude, this maximum sets a limit on the maximum horizontal field there. In particular, the horizontal field does not exceed that induced by two full cycles of rotation. This limit indicates that reconnection is highly efficient at keeping the field not far from its potential state. We found in previous work (Knizhnik et al. 2015; Zhao et al. 2015) that for the 100% case, reconnection sets in well before the flux tubes acquire two turns of twist. For the 0% case, two full twists are generally sufficient to induce kinking of the flux tubes, which again results in efficient reconnection. In any event, since the whole flow pattern is rotated randomly after each cycle, current sheets and reconnection will inevitably appear during the second cycle, irrespective of the helicity preference.

There are a number of important features in the Poynting flux maps. First we note that, as with the temperature, the three cases show marked differences at the boundary. For the 0% case, there is no significant difference between the fluxes at the center versus the boundary; the pattern appears to be roughly random everywhere. The 100% case, on the other hand, shows distinct structure at the boundary, particularly in the last row of photospheric rotation cells. At the outer edge of each of these cells, the flux is strongly positive, whereas it is negative at the inner edge. It is straightforward to understand this pattern. At the outer edge, the flow is in the direction that increases the large-scale shear of the filament channel field; consequently, it injects a large, positive Poynting flux there. At the inner edge, in contrast, the flow acts to decrease the shear, resulting in a negative Poynting flux. We emphasize that the buildup of large-scale shear is *not* due to this systematic pattern in the outermost cells. Each cell acts only to impart a localized rotation of its corresponding flux. In other words, a cell at the boundary does not increase the large-scale shear, it only produces a localized twist in the shear flux. If there were no reconnection, no large-scale shear would ever build up. The reconnection causes the small-scale twist flux to cancel in the interior and to build up systematically at the boundary.

The 50% case is intermediate to the other two. There is mainly strong positive flux at the outer edge, but since 1/3 of the rotations are counter-clockwise, there is also some strong negative Poynting flux. Note that even if we ran this case for twice as long as the 100% case, so that the same amount of shear flux builds up at the boundary, the 50% case would still exhibit a mixture of positive and negative Poynting flux.

Figure 3 shows that there are also clear differences between the three cases in the interior of the driven region.

As with the temperature (Fig. 2), the 100% case shows the least structure. All the interior cells appear to be injecting a primarily positive energy flux of intermediate magnitude. In fact, it is surprising how little negative flux is present in the map, given that the whole pattern rotates randomly after every cycle, so that some of the motions should be de-stressing the field. The other two cases exhibit distinct regions of negative Poynting flux, but again primarily positive. Even for the 0% case, where each cell has a random sense of rotation, the Poynting fluxes are primarily positive. This result is critically important, because a net positive flux is required for continued coronal heating.

The results in Figure 3 can be explained by the detailed structure of the magnetic field. As discussed above, reconnection is very efficient at preventing the field from deviating far from its potential state. When the reconnection is pervasive, the Poynting maps should resemble that of panel (a), and the flux density should be positive everywhere. As shown in KAD17, the 100% helicity injection case produces a magnetic field that has the least amount of small-scale structure, and is closest to the potential state. Consequently, the interior region of the Poynting map in panel (b) is quite similar to that of panel (a): there is weak positive flux everywhere (note the scale change between these two panels). For the other two cases, in contrast, the field has some localized regions of strong non-potentiality, so the Poynting maps show locations of strong negative and positive flux. For the most part, nevertheless, the field is sufficiently near potential that the Poynting flux density is weakly positive overall.

In order to understand the effect of spatial variations of the Poynting maps on coronal heating, we calculated the total energy injected into the domain. Area integrations of the flux density S_n over the top and bottom boundaries ($x = 0, 1$) yield the total Poynting fluxes P_n of electromagnetic energy per unit time,

$$P_n(t) = \oint_S S_n(x, y, z, t) dA, \quad (3.3)$$

which are shown in Figure 4a. The dominant temporal behavior of the total Poynting flux is sinusoidal, as determined by the oscillatory nature of the convective cells described in §2. We note that, for the most part, the magnitude of the peak flux varies with the helicity preference. The 100% case shows the highest peak in most cycles, followed by the 50% case, and then the 0%. The actual magnitudes, however, vary significantly from cycle to cycle, and there are even cycles where the 0% case exhibits the highest peak. This result demonstrates the random nature of the driving and the reconnection response. Presumably, we would obtain fewer such fluctuations if we employed a much larger number of driving cells than the 61 used in these simulations, but the temporally averaged results would be similar.

Another important feature of Figure 4a is that the peak flux does not show much of an increase after the first cycle or so. This again implies that the field never deviates much from its initial potential state, except at the ‘‘PIL.’’ To quantify the long-term evolution of the system, we plot the cycle-averaged values $\langle P_n \rangle$ in Figure 4b. After about five cycles, the $p = 0\%$ case appears to have reached a statistically steady state in which the

energy injected is approximately constant from cycle to cycle, albeit with substantial fluctuations. The average flux over the simulation is

$$\langle P_n \rangle_{0\%}^s \approx 5.4 \times 10^{-2}, \quad (3.4)$$

where the superscript s indicates the quasi-steady value. The associated average Poynting flux density is

$$\langle S_n \rangle_{0\%}^s \approx 9.0 \times 10^{-3}. \quad (3.5)$$

The fact that this case achieves a steady state is not surprising. Eventually, the small-scale magnetic stresses in the corona must build up to the point where further tangling simply results in faster energy release by reconnection, leading to a steady state, exactly as predicted by Parker (1972) in his seminal work. What is surprising, perhaps, is how quickly this state is achieved, after only a few cycles of driving. As argued by Parker and by many others (e.g., van Ballegooijen 1985), random footpoint motions are highly efficient at forming current sheets in three dimensions.

As is to be expected, the cases with net helicity injection do not reach a steady state; instead, they exhibit a weak quasi-linear growth at later times. The origin of this trend is the constant increase of the global shear field (the filament channel) at the system boundary, which continuously increases the free energy in the system. This shear field exerts a systematic stress at the photosphere that increases monotonically as the shear field increases. Also as expected, the effect of the global shear field is stronger in the 100% case than in the 50%. To determine this effect more accurately, we plot in Figure 4c the time-integrated Poynting flux, i.e., the total energy injected into the system, for the three cases. Note that the 0% case shows a linear increase with time, whereas the other two curve upward, indicating that the Poynting fluxes for these cases is not constant. Furthermore, the 100% curve shows a stronger upward curvature than the 50% case.

3.3. Magnetic Energy

In order to determine the effect of the photospheric driving motions on the coronal energetics, we calculated the evolution of the total magnetic and plasma energies. The magnetic (free) energy added to the volume is

$$\Delta M(t) = \frac{1}{8\pi} \int_V [B^2(x, y, z, t) - B^2(x, y, z, 0)] dV \quad (3.6)$$

and is displayed in Figure 4d. The oscillatory pattern in each curve is due to the sinusoidal temporal profile of the driving motions. Clearly, the magnetic energy depends strongly on the helicity preference. For the 0% case, the free energy levels off after a dozen cycles or so to a fairly low level that corresponds to $\approx 30\%$ of the initial potential energy. The conclusion is that, after the initial magnetic energy rise, all the Poynting flux is converted to plasma thermal energy.

The two cases with a helicity preference exhibit a clear continued rise in magnetic free energy. The $p = 100\%$ case, for example, has more than triple the free energy of the $p = 0\%$ case, and almost double that of the $p = 50\%$ case. The differences in the free energies, and the relatively large free energy of the 100% case, are due primarily to the highly sheared filament channel that forms

at the boundary of the driven region. This can be seen from the following analysis.

For $p = 100\%$, the magnetic free energy in the corona at the end of the simulation can be estimated by approximating the final configuration as a uniform vertical field everywhere except for a band of global shear flux encircling the outer boundary. The free energy contained in the volume is dominated by the shear field at this boundary, since it is the only location where the magnetic field is highly nonpotential. With this approximation, the free energy of the final configuration for the 100% preference, after 20 cycles, is given by

$$\Delta M_{100\%}^{20} \approx \frac{B_\phi^2}{8\pi} V_b. \quad (3.7)$$

Here V_b is the volume occupied by the band of twist field, whose strength is B_ϕ . The band is centered at distance a_b from the central axis, its width is w , and its height is L_x , so its volume is

$$V_b \approx 2\pi a_b w L_x. \quad (3.8)$$

The twist field strength is given by

$$B_\phi = \frac{\Phi_{tw}}{w L_x}, \quad (3.9)$$

where Φ_{tw} is the twist flux through a vertical plane. In KAD15 we related the twist flux to the helicity injected into the corona, so that, at each instant, Φ_{tw} is known. Substituting Eqs. 3.8 and 3.9 into Eq. 3.7 yields

$$\Delta M_{100\%}^{20} \approx \frac{a_b}{4w L_x} \Phi_{tw}^2. \quad (3.10)$$

Inserting the domain height $L_x = 1$ and the empirical simulation values $w = 0.3$ and $a_b = 1.0$, we find

$$\Delta M_{100\%}^{20} \approx 8.3 \times 10^{-1} \Phi_{tw}^2. \quad (3.11)$$

For $p = 100\%$, KAD15 predicted and confirmed numerically that the twist flux Φ_{tw} depends only upon the amount of helicity injected per convection cell, which for this case satisfies

$$\Phi_{tw} = 1.7 \times 10^{-2} \left[t - \frac{\tau}{2\pi} \sin \left(2\pi \frac{t}{\tau} \right) \right]. \quad (3.12)$$

After 20 cycles, $t = 20\tau$, we find

$$\Phi_{tw} = 1.16. \quad (3.13)$$

Using this value in Eq. 3.11 yields finally

$$\Delta M_{100\%}^{20} \approx 1.12. \quad (3.14)$$

This value agrees quite well with the $p = 100\%$ (orange) curve in Figure 4d. Note that it also is close to the initial magnetic energy in the volume, $M(0) = 1.125$, indicating that our approximation is starting to break down. Once the shear energy becomes of order the initial energy, then the presence of the shear will produce significant displacements in the initially uniform vertical field, thereby increasing the energy in that component as well. This is evident from Figure 2b. Furthermore, our shear field has built up to “too high” a value compared to actual coronal fields. Both theory and observations of CMEs and coronal jets have consistently found that

eruption invariably occurs when the free energy reaches 50% or so of the initial potential energy (e.g., Antiochos et al. 1999; Karpen et al. 2012; Wyper et al. 2017).

As further evidence that the free energy in our system is due primarily to the buildup of the filament channel, we plot in Figure 5 the quantity

$$\Delta M_h(r, t) = \frac{1}{8\pi} \int_0^{2\pi} d\phi \int_0^{L_x} \mathbf{B}_h^2(x, r, \phi, t) dx \quad (3.15)$$

at the end of the simulation for each of the three cases. This quantity is simply the energy density of the horizontal field integrated over height and azimuth for cylindrical shell of radius r . Its distribution shows precisely where the magnetic free energy is stored as a function of distance from the center of the region. We neglect the contribution from the vertical field, which contains minimal free energy except near the very end of the 100% case. Especially for the $p = 100\%$ case, but also for the $p = 50\%$ case, most of the free energy is stored near the boundary of the driven region. In sharp contrast, for $p = 0\%$ the magnetic free energy is spread relatively uniformly throughout the driven region, and it is much smaller than the peak values obtained for $p = 100\%$ and $p = 50\%$. It is tempting to infer from our results that most of the free energy in the solar corona is stored in filament channels, but some caution needs to be taken here due to the geometrical differences between the corona and our closed-box domain. Observations clearly show that the strong non-potentiality of the coronal field (i.e., any electric current) is highly concentrated in the filament channel, as in our simulation. However, since the corona is an infinite domain in which the field generally drops off rapidly with height, the presence of a filament channel causes large upward displacements and increases the free energy of the overlying flux. This is inherent in all CME models: the extra magnetic pressure of the filament field must be balanced by an increased magnetic tension in the overlying flux (Antiochos et al 1999). In our system, the side and top walls of the simulation box can exert confining forces, but, of course, there are no walls in the corona.

3.4. Internal Energy

The results above demonstrate that the helicity preference of the driving motions has a strong effect on the magnetic energy in the corona. It would seem likely, therefore, that it should also have a similar effect on the plasma energy, but this is not the case. The increase in internal energy in the volume is given by

$$\Delta I(t) = \int_V [U(x, y, z, t) - U(x, y, z, 0)] dV \quad (3.16)$$

and is displayed in Figure 4e. It accounts for more than 75% of the total energy added to the volume even for the 100% helicity preference. Clearly, the majority of the injected energy is converted into heat via magnetic reconnection, rather than remaining stored in the magnetic field. The important result of our study, evident in Figure 4e, is that *the amount of heating is only weakly dependent on the helicity preference*. At least for these particular simulations, the increase in internal energy appears to be almost the same for $p = 100\%$, $p = 50\%$, and $p = 0\%$, especially near the end of the simulations.

This result is somewhat surprising given that the photospheric Poynting fluxes for the three cases show measurable differences. Concentrating on the 100% and 0% cases, we note from Figures 4a and 4b that the Poynting flux for the former case is noticeably higher throughout the evolution than for the latter. In contrast, between about cycles 5 to 12 the internal energy for the 100% case in Figure 4e is only slightly higher than that for the 0%, and the latter catches up by about cycle 16. Over the last 4 cycles of the three simulations, their internal energies are virtually indistinguishable. It seems unlikely that if we were to continue the driving for more cycles beyond 20, a clear separation of the internal energies would appear. Moreover, such a result would be difficult to relate to the corona, because the simulated plasma beta has already risen well above unity by cycle 20.

Although the degree of agreement between the internal energies of the three cases is surprising, the basic result that the heating rate is weakly sensitive to the helicity injection is not unexpected (e.g., Wilmot-Smith et al. 2011). For turbulent 3D MHD systems, both experiment and theory have shown that free energy and helicity undergo very different evolutionary tracks: the energy cascades down to the dissipation scale where it is converted to thermal energy, while the helicity cascades up in scale and simply collects there (e.g., Biskamp 1993). Of course, our system is not truly turbulent. The line-tying at the photosphere and the low plasma beta restrict the corona from undergoing an actual turbulent cascade wherein eddies of continuously decreasing scale are spontaneously generated by large-scale driving. The corona, however, does not require turbulence for its heating, only ubiquitous reconnection, and this is exactly what the line-tying and the low beta produce.

A priori, it would seem likely that the free-energy evolution of the three cases would be quite similar. The energy is injected by small-scale quasi-random motions with the same scale, speed, etc. and, except for the filament channel, the coronal field remains rather close to the potential state. The differences in the heating, therefore, are likely to be small. If anything, we would expect the 100% case to have the lowest heating, because the driving is such that it is maximally efficient at inducing reconnection. In other words, this case has the largest effective resistivity and, as argued many years ago by Parker (1972), a larger resistivity results in a smaller heating rate.

To investigate this hypothesis quantitatively, we plot in Figure 4f the time-integrated Poynting flux through the boundaries, analogous to Figure 4c, but for subregions on the boundaries. In order to make direct comparison easier, we plot the flux per unit area and, to reduce clutter, we include only the 0% (blue) and 100% (orange) cases. The dashed curves represent the region $0.75 < r < 1.0$, which corresponds to the filament channel, and the solid curves represent the main interior region $0.25 < r < 0.75$. We omit the exact center because it is somewhat artificial, in that the twist there is never displaced by the random rotation of the pattern.

The first result to note from Figure 4f is that the integrated flux per area in the filament channel region is much larger for the 100% case than for the 0%. This is to be expected from comparison of Figures 3b and 3d. The rotations in the outermost ring for the 100% case show a

substantially larger positive Poynting flux than negative, especially for those rotations along the sides of the hexagonal pattern. These rotations intersect the boundary of the filament channel region, so the flow along their outer edges moves in the direction of the shear and provides a strong positive Poynting flux, while their inner edges are in the weak-shear zone and produce only a weak negative. For the 0% case, on the other hand, the Poynting flux is randomly distributed along each flow irrespective of the flow’s location. The enhanced Poynting flux in the vicinity of the filament channel for the 100% case provides the energy for the shear field there, and indirectly enhances the internal energy throughout the volume. Recall that the temperature in the interior is systematically larger in this case due to the “squeezing” of the interior by the band of strong shear flux. We conclude that if the only driving were in the outer ring, $0.75 < r < 1.0$, the internal energy of the 100% case would be larger than that of the 0%.

The driving in the interior region, however, has the opposite effect. Figure 4f shows that in the region $0.25 < r < 0.75$, the Poynting flux per area is significantly larger for the 0% case than the 100%. The reason is simply the lack of large-scale twisting and tangling that develop for 100% helicity injection, as discussed in KAD17. Figure 6 shows the variations in the magnitude of the horizontal magnetic field,

$$B_h = \sqrt{B_y^2 + B_z^2}, \quad (3.17)$$

at the bottom boundary for the three cases. We actually plot the total B but, since the vertical component stays uniform throughout the simulations, the contours in Figure 6 reflect B_h . The 100% case exhibits the strong B_h ring of the filament channel, but almost no B_h structure in the interior. Reconnection is amazingly efficient at “transporting” all the helicity to the PIL, leaving a very smooth coronal-loop region. The 0% case, in sharp contrast, contains clumps of large B_h located randomly throughout the driven region. Since the Poynting flux is directly proportional to B_h , the flux is noticeably larger for the smaller helicity preference.

In applying these results to the observed corona, a number of effects must be kept in mind. First, the ratio of the areas of the filament channel versus coronal-loop regions will vary, thereby changing the cumulative agreement evident in Figure 4e. For example, if we were to double the radius of our system, but keep the size of each photospheric rotation the same, then the area of the filament channel would double, but the area of the interior (coronal loop) region, along with the number of rotations, would increase by a factor of four. In this case, a large helicity injection preference would result in a cooler corona with less internal energy. Another effect is that magnetic flux in the corona can expand outward and, hence, change the internal energy of the plasma. The buildup of the filament channel will cause the overlying coronal-loop flux to expand upward, thereby decreasing B_h at the photosphere and the resulting Poynting flux.

The final important effect is that of numerical resolution. For our simulations, in which the effective resistivity is numerical, the scale of the grid determines the dissipation scale. As we increase the refinement level of the simulations, we expect the effective resistivity to de-

crease and, consequently, the heating to increase. This will likely enhance any differences in the heating rates between the different cases. The scaling of the heating with numerical resolution is also a critical issue for applying our results quantitatively to the observed corona. Therefore, in the following section we discuss in detail the effect of numerical resolution.

4. GRID-RESOLUTION STUDY

The key question for our study is, how do the heating rates in our calculations compare to the observed coronal heating? The main challenge with addressing this question using any simulation is that the numerical Lundquist numbers are inevitably far lower than those in the corona. Consequently, the best that can be done is to perform a scaling study and attempt to extrapolate to coronal parameters. In our calculations, the conversion of injected magnetic energy into plasma heating and internal energy occurs via magnetic reconnection across current sheets formed at the numerical grid scale; therefore, in order to scale on our results with effective Lundquist number, we performed simulations at several different grid resolutions. To avoid the complication of contributions from the filament channels, we elected to conduct this study for the $p = 0\%$ case. We used four different levels of refinement, denoted by $l = 1, 2, 3$, and 4, corresponding to 8, 16, 32, and 64 grid points across each rotation cell, respectively. The results presented in §3 were obtained with $l = 3$, or 32 grid points across each cell.

The first five panels (a-e) of Figure 7 display the same quantities as the corresponding panels in Figure 4, but for fixed $p = 0\%$ at the different refinement levels $l = 1, \dots, 4$. In general, all quantities increase as the refinement level increases. The instantaneous, time-averaged, and time-integrated Poynting fluxes (Fig. 7a-c) exhibit increasing amplitudes and fluctuation levels, reflecting the enhanced small-scale structure and dynamics that follow from the improvements in resolution. These features also are evident in the plots of the magnetic and internal energies (Fig. 7d-e). In contrast to our finding in §3 that the internal energy change, and thus the heating rate, is only weakly dependent on helicity preference p , here we observe that these quantities are quite dependent upon the refinement level l , increasing monotonically as the grid resolution increases. During the first five cycles of rotation, the curves all rise together at essentially the same pace; thereafter, however, they begin to diverge and adopt slightly different slopes, i.e., heating rates.

The last panel (f) of Figure 7 shows the evolution of the internal energies for the 0% (solid) and the 100% (dashed) cases at the highest numerical resolution. We now see a clear deviation between the two, with the 100% helicity preference resulting in a lower heating rate, as expected. The difference is not substantial, however, only of order 15% or so. We conclude that the helicity preference, hence the *net* helicity injection, plays only a minor role in determining the magnitude of the coronal heating.

To analyze and apply our results to the heating of the real corona, we introduce an effective numerical diffusivity into the induction equation η ,

$$\frac{\partial \mathbf{B}}{\partial t} = \nabla \times (\mathbf{v} \times \mathbf{B}) - \nabla \times (\eta \nabla \times \mathbf{B}). \quad (4.1)$$

In our simulation, the energy conversion also involves

dissipation of small-scale mass motions into heat via numerical viscosity. For the purposes of this total energy analysis, we simply lump all the dissipation into the effective resistivity. Taking the numerical heating to be due to an effective resistive dissipation at the reconnection sites, the rate of change of internal energy is

$$\begin{aligned} \frac{dI}{dt} &= \frac{1}{4\pi} \int_V \eta |\nabla \times \mathbf{B}|^2 dV \\ &= \frac{\langle \eta \rangle}{4\pi} \int_V |\nabla \times \mathbf{B}|^2 dV. \end{aligned}$$

We solved this equation for the spatially averaged diffusivity, $\langle \eta \rangle$, averaged the rate of internal energy change over the 20 driving cycles of the simulation,

$$\left\langle \frac{dI}{dt} \right\rangle = \frac{\Delta I_{0\%}^{20}}{20\tau}, \quad (4.2)$$

and calculated the (quasi-periodic) maximum volume integral of $|\nabla \times \mathbf{B}|^2$ late in the simulations. The result is

$$\langle \eta \rangle = 4\pi \frac{\Delta I_{0\%}^{20}}{20\tau} \left[\left\langle \int_V |\nabla \times \mathbf{B}|^2 dV \right\rangle \right]^{-1}. \quad (4.3)$$

We then used these values to calculate the average Lundquist numbers $\langle S \rangle$ for the simulations,

$$\langle S \rangle = \frac{V_A L_x}{\langle \eta \rangle} = \frac{1}{\langle \eta \rangle}, \quad (4.4)$$

in which the background Alfvén speed $V_A = 1$ and the current-sheet length is assumed to be the simulation box height, $L_x = 1$. The resulting data points are displayed in Figure 8 for the Lundquist number $\langle S \rangle$ vs. the reciprocal grid spacing. Also shown as a red line is a linear fits to these points,

$$\langle S \rangle \approx 4.0h^{-1}, \quad (4.5)$$

or, alternatively,

$$\langle \eta \rangle \approx 0.25h. \quad (4.6)$$

The point for the lowest refinement level, $l = 1$, is omitted from the graph and the curve fit because the grid is so coarse that the result deviates significantly (though not anomalously) from the trends set by the highest three levels, $l = 2, 3, 4$. In order to fill out the interval, we performed additional simulations at intermediate resolutions of 24 and 48 grid points per rotation cell, corresponding to refinement levels $l \approx 2.6, 3.6$. The results obtained indicate that the effective diffusivity scales in direct proportion to the grid spacing, as expected for the resolution-dependent numerical diffusion coefficients employed by our algorithm (DeVore 1991). Consequently, the associated Lundquist number scales inversely with the grid spacing.

For each simulation, we calculated the effective heating rate $\langle H \rangle$ (internal energy per unit area per unit time) by dividing the average rate of change of internal energy by the total area (top and bottom plates) occupied by the rotation cells,

$$\langle H \rangle = \frac{1}{2N\pi a_0^2} \left\langle \frac{dI}{dt} \right\rangle. \quad (4.7)$$

These results are displayed vs. the effective Lundquist number $\langle S \rangle$ in Figure 9 as filled circles. We fit a logarithmic curve to these data, obtaining

$$\langle H \rangle = 2.2 \times 10^{-3} (\log S) + 3.2 \times 10^{-3}, \quad (4.8)$$

shown as the solid line in the figure. The fit here is not as tight as those shown in the preceding figure, but it is still reasonably good. This result allows us to extrapolate our numerical results to coronal Lundquist numbers, as described below.

5. SOLAR CORONAL HEATING

The results above can be related quantitatively to observed properties of solar coronal heating. In a statistically steady state, Parker (1983) relates the average coronal heating rate in a system like ours to the inclination angle θ of the field with respect to the vertical,

$$\langle H \rangle = \frac{1}{4\pi} \langle v_h B_n^2 \tan \theta \rangle, \quad (5.1)$$

where v_h is the horizontal driving velocity and B_n is the field component normal to the surface. Solving for the inclination angle, known as the Parker angle (Klimchuk 2015), we obtain

$$\langle \theta_P \rangle = \arctan \left(\frac{4\pi \langle H \rangle}{\langle v_h B_n^2 \rangle} \right). \quad (5.2)$$

Substituting simulation parameters $\langle v_h \rangle \approx 0.5v_h^{\max} = 0.1$, $B_n = \sqrt{4\pi}$, and $\langle H \rangle = 0.010$ for $p = 0\%$ at level $l = 4$, we find

$$\langle \theta_P \rangle = \arctan(0.10) \approx 6^\circ. \quad (5.3)$$

This angle is far smaller than the value $\theta_P = \arctan(0.4) = 22^\circ$ estimated by Parker (1983) to account for the empirically measured heating of the corona. However, we showed above that the results of our grid-resolution study yield a logarithmic scaling law for the heating rate, $\langle H \rangle$, in Eq. (4.8) and Figure 9, vs. Lundquist number S . Extrapolating from our simulated Lundquist numbers $S \sim 10^{3-4}$ to a coronal Lundquist number $S_\odot \sim 10^{12}$, we obtain the much larger nondimensionalized heating rate

$$\langle H \rangle \approx 0.030. \quad (5.4)$$

Substituting this result into Eq. (5.3) for the Parker angle, we find

$$\langle \theta_{P\odot} \rangle = \arctan(0.30) \approx 17^\circ. \quad (5.5)$$

This is much closer to Parker's original estimate of 22° for the corona.

To convert our simulated coronal heating rate to solar values, from Eq. 5.1 we have

$$\frac{\langle H_\odot \rangle}{\langle v_\odot B_\odot^2 \rangle} = \frac{\langle H \rangle}{\langle v_h B_n^2 \rangle} = \frac{1}{4\pi} \langle \tan \theta_{P\odot} \rangle \approx 0.024 \quad (5.6)$$

after substituting our extrapolated Parker angle $\theta_{P\odot}$ for coronal Lundquist numbers S_\odot from Eq. (5.5). The coronal heating rate therefore is

$$\langle H_\odot \rangle \approx 0.024 \langle v_\odot B_\odot^2 \rangle. \quad (5.7)$$

Assuming a photospheric flow speed $v_{\odot} = 1 \times 10^5 \text{ cm s}^{-1}$ and an average quiet-Sun flux density $B_{\odot} = 10 \text{ G}$, we obtain

$$\langle H_{\odot} \rangle_{QS} \approx 2.4 \times 10^5 \text{ erg cm}^{-2} \text{ s}^{-1}. \quad (5.8)$$

This value is in very good agreement with accepted quiet-Sun energy loss rates (Withbroe & Noyes 1977). In active regions, on the other hand, typical average magnetic flux densities are an order of magnitude larger than those in quiet Sun (e.g. Martínez Pillet et al. 1997), so the Poynting flux density is two orders of magnitude larger than the quiet-Sun value above. The resulting heating rate,

$$\langle H_{\odot} \rangle_{AR} \approx 2.4 \times 10^7 \text{ erg cm}^{-2} \text{ s}^{-1}, \quad (5.9)$$

also is in excellent agreement with the observed rate of energy loss from active regions (Withbroe & Noyes 1977).

6. DISCUSSION

In this work, we calculated the effects of helicity injection on the heating of the corona using helicity- and energy-conserving numerical simulations. Helicity was injected into the corona via numerous convective cells at the photosphere, whose sense of rotation and position were randomly varied. In previous papers, we showed that this helicity was transported throughout the simulation domain by magnetic reconnection, forming filament channels (KAD15) and leaving behind a relatively smooth corona (KAD17). In this paper, we explored how magnetic reconnection distributes the injected energy between the magnetic field and the plasma, and we found a number of important results.

The main conclusion is that, irrespective of helicity, the majority of the injected energy is converted into heating, with the rest building up the free energy of the coronal magnetic field. Furthermore, we found that the amount of heating depends only weakly upon the helicity preference. It seems unlikely, therefore, that the helicity preference of the photospheric motions can be inferred from measurement of the coronal heating rate. On the other hand, the amount of energy remaining in the magnetic field depends strongly upon this preference, with the most magnetic energy remaining in the field for larger helicity preferences. Given the observed ubiquitous formation of filament channels in the corona, along with the frequent coronal mass ejections, it seems highly likely that the photospheric convective motions inject a net helicity into the corona Mackay et al. (e.g. 2018). Furthermore, our results imply that current-sheet formation and reconnection are most efficient for maximal helicity preferences and least efficient for negligible helicity preferences. This conclusion is in line with previous studies of flux tube dynamics (e.g. Zhao et al. 2015). Crucially, we also showed quantitatively that the resulting energy flux into the corona can account for the observed heating. This result agrees with the many studies, dating back to Parker (1972), that the observed photospheric convective flows and photospheric field strengths are sufficient to heat the corona.

Taken together with KAD15 and KAD17, the results of this paper constitute a comprehensive model for helicity injection into the corona. In this model, surface motions inject free energy and helicity into the solar corona. The helicity is transported to the largest available scales by

magnetic reconnection where it is lost only through occasional explosive ejections, while most of the energy is converted to heat. The single process of magnetic helicity condensation, therefore, can simultaneously explain the formation of filament channels that lead to coronal ejections, the smoothness of coronal loops, and the heating of the Sun’s multi-million degree corona.

Our study also suggests that the reconnection responsible for helicity condensation should be explored in more detail. Does such reconnection proceed as a series or, perhaps, a storm of nanoflares (Klimchuk 2015)? Or is the reconnection, instead, a single, spontaneous event? Another important issue to be explored is the relation between the size of the individual reconnection events – the nanoflares – and the properties of the photospheric driving. Future work also should address the influence of the magnetic topology, in configurations having true PILs such as the bipolar sunspot simulated by Knizhnik et al. (2017b), on the rate and distribution of coronal heating. Irrespective of the resolution of these issues, however, it is clear from our study, and many others, that the injection and transport of magnetic energy and helicity play major roles in determining the structure, dynamics, and heating of the solar corona.

K.J.K. gratefully acknowledges funding for this work received through a NASA Earth and Space Science Fellowship, as well as the use of codes written by B. J. Lynch. The numerical simulations were performed under a grant of NASA High-End Computing resources to C.R.D. on Discover at NASA’s Center for Climate Simulation. Grants from NASA’s Living With a Star, Heliophysics Supporting Research, and Heliophysics Internal Scientist Funding Model programs partially supported K.J.K., S.K.A., J.A.K., and C.R.D.

REFERENCES

- Antiochos, S. K. 2013, *ApJ*, 772, 72
- Antiochos, S. K., DeVore, C. R., & Klimchuk, J. A. 1999, *ApJ*, 510, 485
- Berger, M. A. 1984, *GApFD*, 30, 79
- Biskamp, D. 1993, *Nonlinear Magnetohydrodynamics* (New York: Cambridge Univ. Press)
- Bradshaw, S. J., Klimchuk, J. A., & Reep, J. W. 2012, *ApJ*, 758, 53
- Bonet, J. A., Márquez, I., Sánchez Almeida, J., Cabello, I., & Domingo, V. 2008, *ApJ*, 687, L131
- Cargill, P. J. 1994, *ApJ*, 422, 381
- Cirtain, J. W., Golub, L., Winebarger, A. R., et al. 2013, *Natur*, 493, 501
- Dahlburg, R. B., Einaudi, G., Taylor, B. D., et al. 2016, *ApJ*, 817, 47
- DeVore, C. R. 1991, *JCoPh*, 92, 142
- DeVore, C. R., & Antiochos, S. K. 2008, *ApJ*, 680, 740
- Duvall, T. L., Jr., & Gizon, L. 2000, *SoPh*, 192, 177
- Gerrard, C. L., Arber, T. D., & Hood, A. W. 2002, *A&A*, 387, 687
- Gizon, L., & Duvall, T. L., Jr. 2003, in *ESA Special Pub. 517, GONG 2002, Local and Global Helioseismology: The Present and Future*, ed. H. Sawaya-Lacoste (Noordwijk: ESA), 43
- González-Avilés, J. J., & Guzmán, F. S. 2015, *MNRAS*, 451, 300
- Grottrian, W. 1939, *NW*, 27, 214
- Hahn, M., & Savin, D. W. 2014, *ApJ*, 795, 111
- Karpen, J. T., Antiochos, S. K., & DeVore, C. R. 2012, *ApJ*, 760, 81
- Klimchuk, J. A. 2006, *SoPh*, 234, 41
- Klimchuk, J. A. 2015, *RSPTA*, 373, 40256
- Knizhnik, K. J., Antiochos, S. K., & DeVore, C. R. 2015, *ApJ*, 809, 137
- Knizhnik, K. J., Antiochos, S. K., & DeVore, C. R. 2017, *ApJ*, 835, 85
- Knizhnik, K. J., Antiochos, S. K., DeVore, C. R., & Wyper, P. F. 2017, *ApJ*, 851, L17
- Knizhnik, K. J., Uritsky, V. M., Klimchuk, J. A., & DeVore, C. R. 2018, *ApJ*, 853, 82
- Komm, R., Howe, R., Hill, F., et al. 2007, *ApJ*, 667, 571
- Kruskal, M., & Schwarzschild, M. 1954, *RSPSA*, 223, 348
- Kumar, N., Kumar, P., & Singh, S. 2006, *A&A*, 453, 1067
- Linton, M. G., Fisher, G. H., Dahlburg, R. B., & Fan, Y. 1999, *ApJ*, 522, 1190
- Linton, M. G., & Antiochos, S. K. 2002, *ApJ*, 581, 703
- Mackay, D. H., DeVore, C. R., Antiochos, S. K., & Yeates, A. R. 2018, *ApJ*, 869, 62
- Mackay, D. H., Karpen, J. T., Ballester, J. L., Schmieder, B., & Aulanier, G. 2010, *SSRv*, 151, 333
- Martínez Pillet, V., Lites, B. W., & Skumanich, A. 1997, *ApJ*, 474, 810
- Osterbrock, D. E. 1961, *ApJ*, 134, 347
- Parker, E. N. 1972, *ApJ*, 174, 499
- , 1983, *ApJ*, 264, 642
- Pekünlü, E. R., Çakırlı, Ö., & Özetken, E. 2001, *MNRAS*, 326, 675
- Peter, H., Bingert, S., Klimchuk, J. A., et al. 2013, *A&A*, 556, A104
- Pevtsov, A. A., Balasubramaniam, K. S., & Rogers, J. W. 2003, *ApJ*, 595, 500
- Pontin, D. I., Wilmot-Smith, A. L., Hornig, G., & Galsgaard, K. 2011, *A&A*, 525, A57
- Rappazzo, A. F., Velli, M., & Einaudi, G. 2013, *ApJ*, 771, 76
- Schrijver, C. J., Title, A. M., Berger, T. E., et al. 1999, *SoPh*, 187, 261
- Seligman, D., Petrie, G. J. D., & Komm, R. 2014, *ApJ*, 795, 113
- Shafranov, V. D. 1956, *At. Energy*, 5, 38
- Taylor, J. B. 1974, *PhRvL*, 33, 1139
- , 1986, *RvMP*, 58, 741
- Török, T., Kliem, B., & Titov, V. S. 2004, *A&A*, 413, L27
- van Ballegoijen, A. A. 1985, *ApJ*, 298, 421
- Vargas Domínguez, S., Palacios, J., Balmaceda, L., Cabello, I., & Domingo, V. 2015, *SoPh*, 290, 301
- Viall, N. M., & Klimchuk, J. A. 2011, *ApJ*, 738, 24
- Welsch, B. T. 2015, *PASJ*, 67, 18
- Wilmot-Smith, A. L., Pontin, D. I., Yeates, A. R., & Hornig, G. 2011, *A&A*, 536, A67
- Withbroe, G. L., & Noyes, R. W. 1977, *ARA&A*, 15, 363
- Woltjer, L. 1958, *PNAS*, 44, 489
- Wyper, P. F., Antiochos, S. K., & DeVore, C. R. 2017, *Natur*, 544, 452
- Zhao, L., DeVore, C. R., Antiochos, S. K., & Zurbuchen, T. H. 2015, *ApJ*, 805, 61

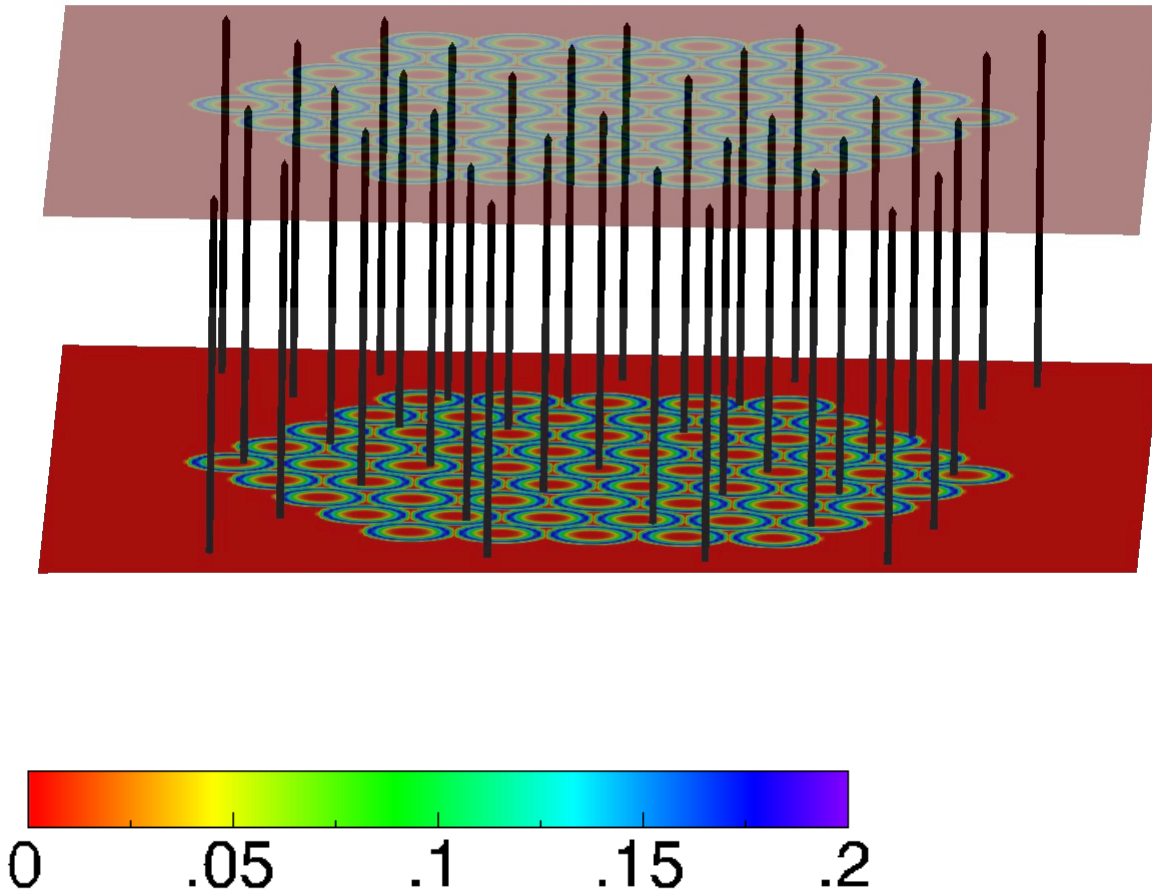


Figure 1. Setup of the numerical simulations. Black lines represent the initial vertical magnetic field; color shading on the top and bottom plates represents velocity magnitude. To emulate the random photospheric convection in our numerical experiments, the local sense of rotation (clockwise/counter-clockwise) of individual convective cells shown in this figure is set randomly for helicity preferences $p \neq 100\%$, and the global hexagonal pattern of the cells collectively is rotated randomly about its center for all helicity preferences.

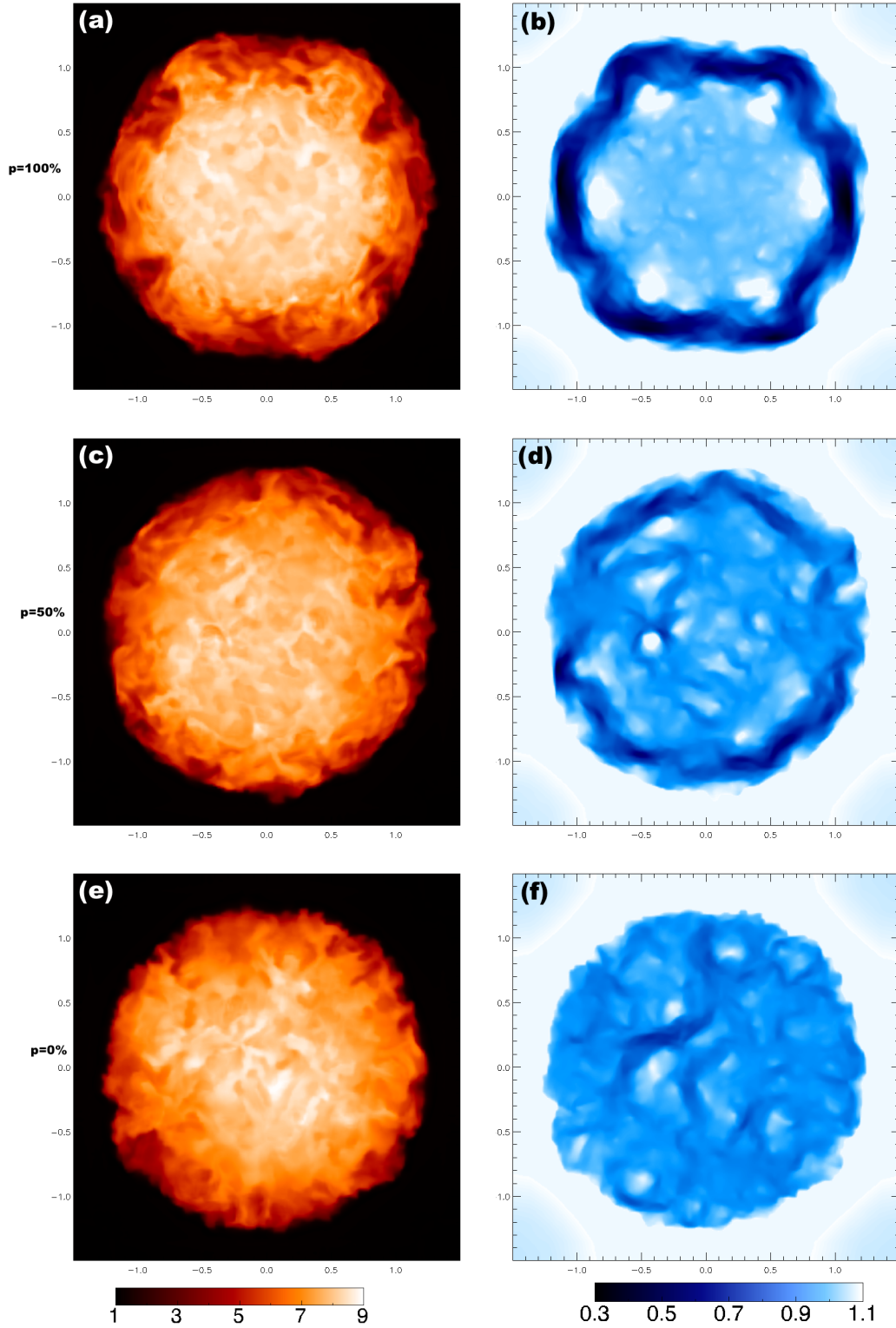


Figure 2. Temperature (left) and B_x/B_0 (right) in the midplane at the end of the simulation for the $p = 100\%$ (top), $p = 50\%$ (middle), and $p = 0\%$ (bottom) preferences.

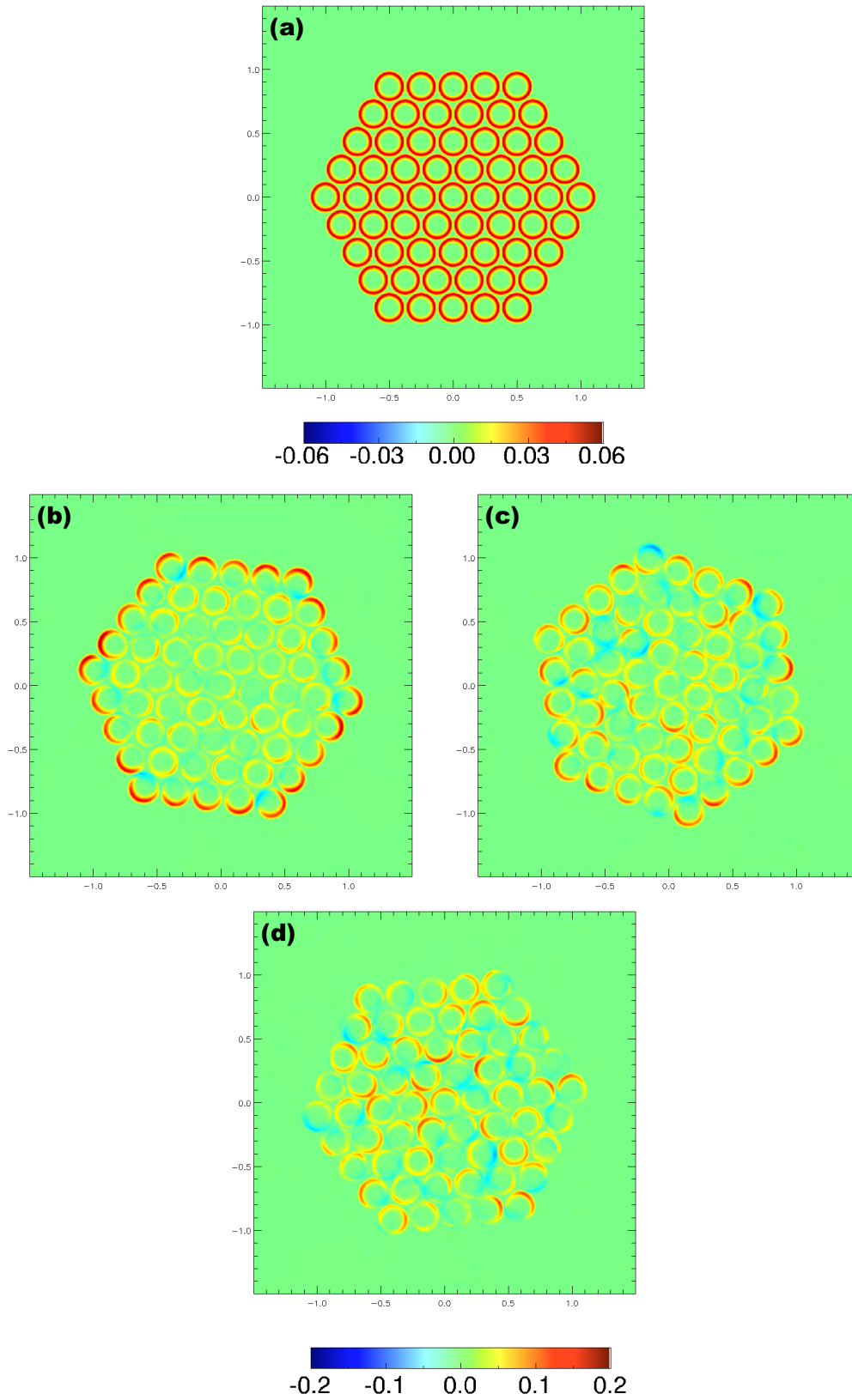


Figure 3. Poynting flux on the bottom plate in the middle of the first cycle (a) for each simulation, and during the last cycles for the $p = 100\%$ (b), $p = 50\%$ (c), and $p = 0\%$ (d) preferences.

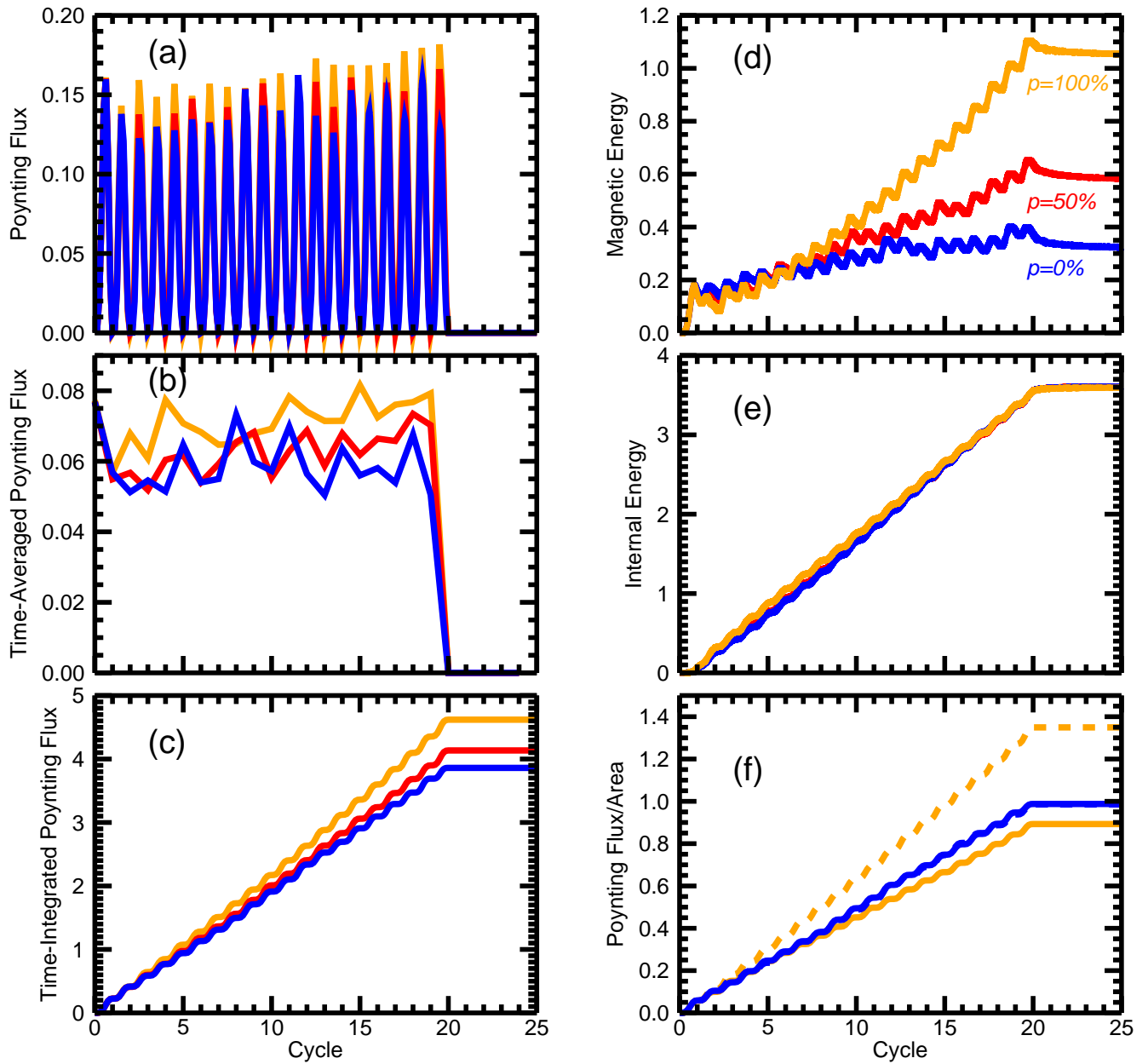


Figure 4. Left: Instantaneous (a), cycle-averaged (b), and time-integrated (c) Poynting fluxes vs. time for the $p = 100\%$ (orange), $p = 50\%$ (red), and $p = 0\%$ (blue) preferences. Right: Corresponding free magnetic (d), and excess internal (e) energy. In (f), we plot the Time-Integrated Poynting flux per unit area inside disks of radii $0.25 < r < 0.75$ (solid curves) and $0.75 < r < 1.00$ (dashed curves) for the $p = 100\%$ and $p = 0\%$ cases. Note that the dashed blue line is completely covered by the solid blue line.

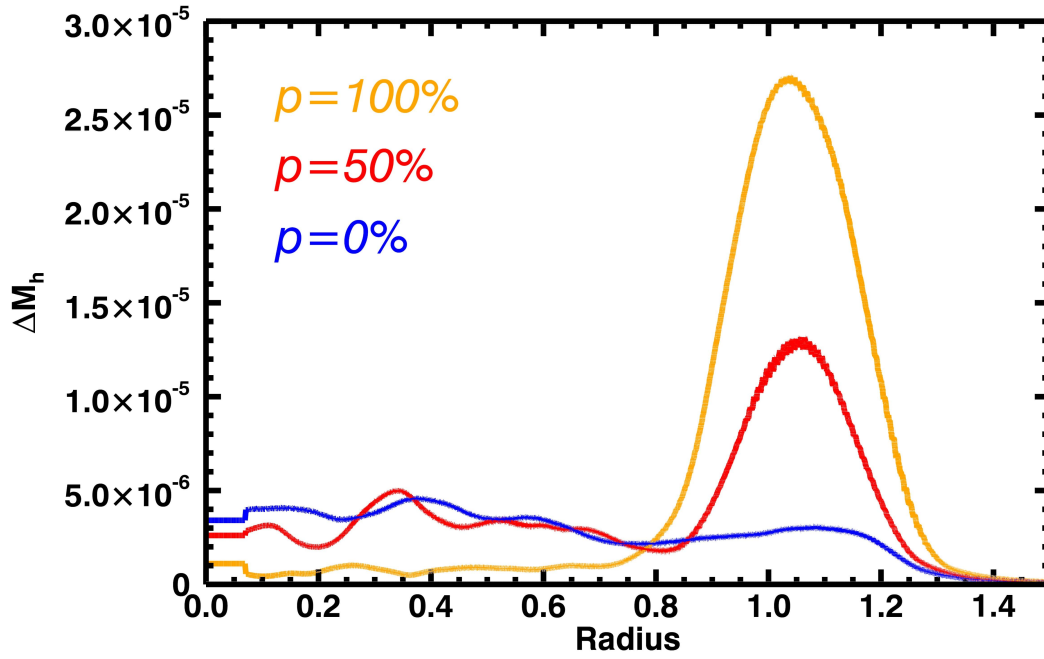


Figure 5. Free magnetic energy density, integrated vertically and azimuthally, vs. radius at the end of the simulation for the $p = 100\%$ (orange), $p = 50\%$ (red), and $p = 0\%$ (blue) preferences. (cf. Eq. 3.15).

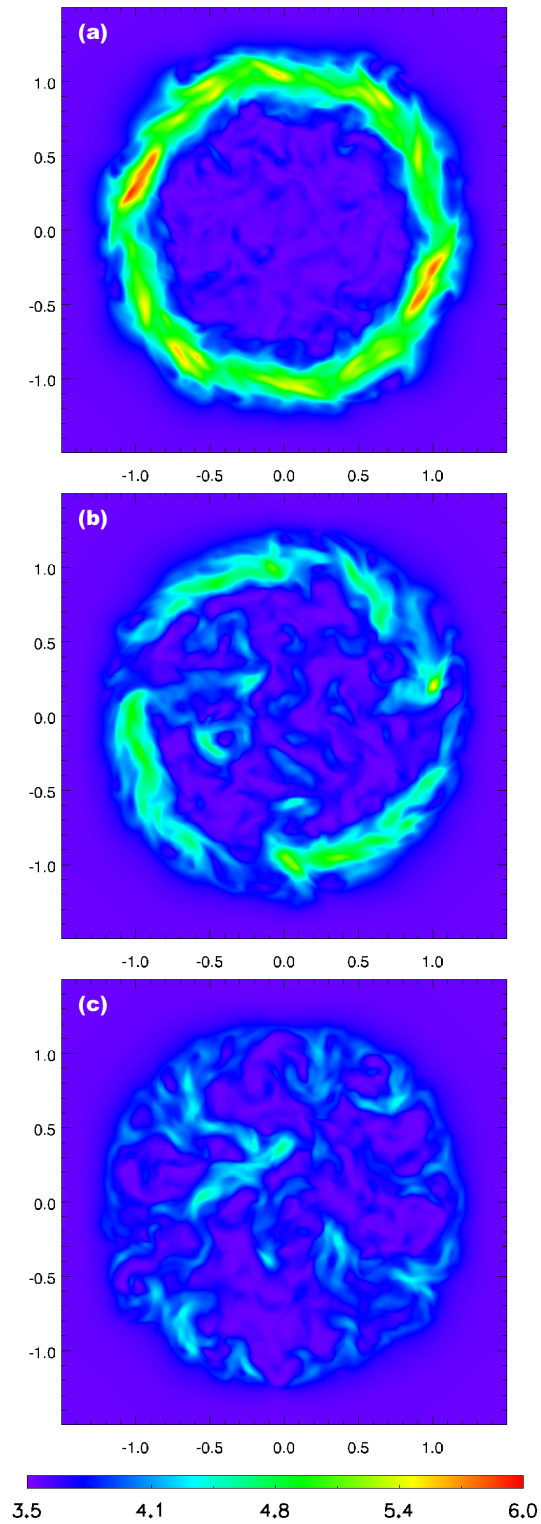


Figure 6. $|B|$ at the bottom boundary at the end of the simulation for the (a) $p = 100\%$, (b) $p = 50\%$ and (c) $p = 0\%$ preferences.

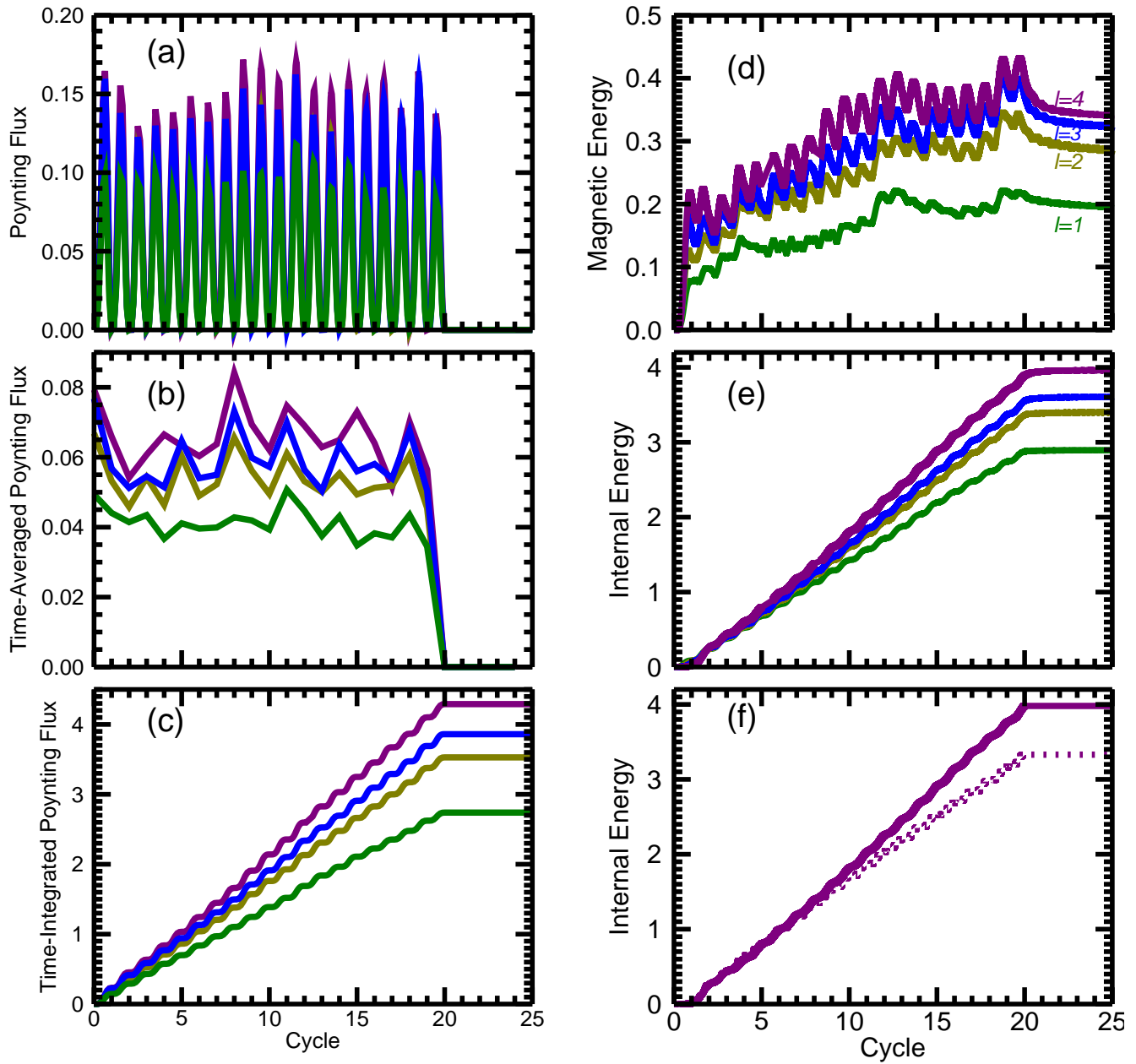


Figure 7. Left: Instantaneous (a), cycle-averaged (b), and time-integrated (c) Poynting fluxes vs. time for the $p = 0\%$ preference for simulations at refinement levels $l = 1$ (green), $l = 2$ (olive), $l = 3$ (blue), and $l = 4$ (purple). Right: Corresponding free magnetic (d), excess internal (e), and excess total energy. (f) shows the excess internal energy for the $l = 4$ 0% (solid) and 100% (dashed) helicity cases.

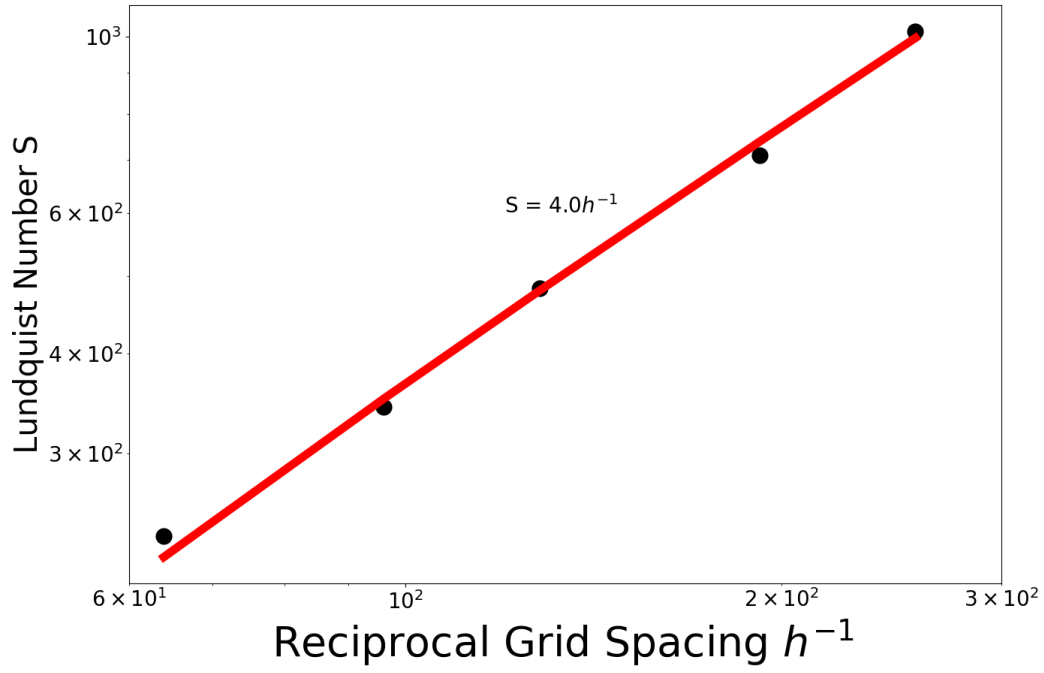


Figure 8. Average Lundquist number versus reciprocal grid spacing (h^{-1}) for the three simulations with $l = 2, 3, 4$, along with two intermediate resolution cases $l \approx 2.6, 3.6$. Also plotted is the line of best fit for the Lundquist number versus h .

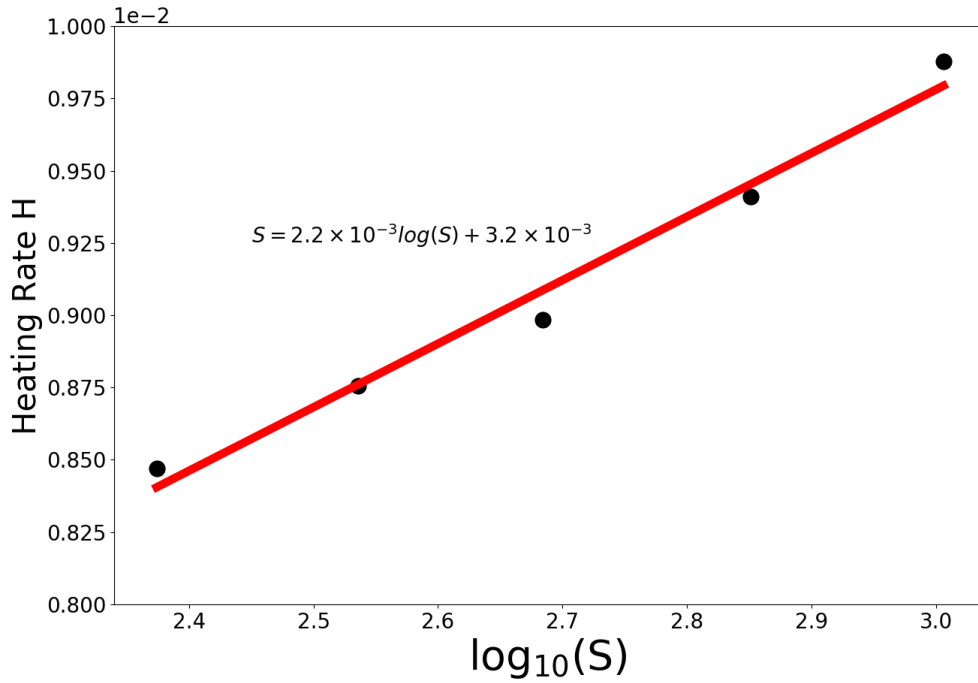


Figure 9. Heating rate versus Lundquist number for the three simulations with $l = 2, 3, 4$, as well as two intermediate-resolution cases $l \approx 2.6, 3.6$, along with a line of best fit.